# The statistics of microlensing light curves – II. Temporal analysis

G. F. Lewis[1]★ and M. J. Irwin[2]

[1]*Institute of Astronomy, Madingley Road, Cambridge CB3 0HA*
[2]*Royal Greenwich Observatory, Madingley Road, Cambridge CB3 0EZ*

**ABSTRACT**
Microlensing at cosmological distances can induce violent fluctuations in the observed light curves of macrolensed quasars. In a previous publication the amplification probability distributions for a large sample of microlensing light curves were presented. This paper extends these earlier results and presents a temporal analysis for this light-curve sample. The temporal properties are explored using the first-order structure function. The results of this study show that (1) the asymptotic global curvature of the structure function depends on the macrolensing parameters $\sigma_*$ and $\gamma$ and not on the detail of the mass distribution, (2) the characteristic time-scale for variability due to microlensing is $\propto \sqrt{\langle m \rangle}$, where $\langle m \rangle$ is the average mass of the microlensing objects, and again does not depend on the detailed shape of the mass distribution, and (3) the structure function time-scale does not vary with shear angle as a purely geometric transformation, but does possess an underlying symmetry solely dependent on the macrolensing parameters. A comparison of simulations of the quadruple lens, $2237 + 0305$, with the currently available temporal light curves suggests that the average mass distribution of the lensing objects in $2237 + 0305$ is within the range $0.1 < \langle m \rangle < 10 \, M_\odot$.

**Key words:** methods: numerical – gravitational lensing.

## 1 INTRODUCTION

The effects of a single, solar-mass star on the light beam of a distant quasar were first investigated by Chang & Refsdal (1979). Although the image splitting was found to be unobservable, $\sim 10^{-6}$ arcsec, it was seen that the lensing amplification could be substantial and would result in fluctuations in the observed light curve of a macrolensed quasar. In realistic macrolensed objects this single-star approximation is invalid, as many microlenses will affect the passage of a light ray through a galaxy. As this number of stars can be large, analytic solutions of the ray-tracing become intractable, and simulations of microlensing have to be tackled numerically.

The workhorse for simulating microlensing light curves has been the backwards ray-tracing technique (Kayser, Refsdal & Stabell 1986; Schneider & Weiss 1987). With this, a regular grid of light rays are traced from an observer, through a plane of lensing objects and into a source plane. The distribution of the rays over the source plane constitutes an amplification map, indicating the brightness of a

resultant image at various positions of a source. This method requires many rays to be traced through the lens plane and is very time-consuming. In general, only a single realization is generated per parameter set. These synthetic light curves did show that in the many-star regime a microlensed quasar will show complex and violent fluctuations.

Recently, the development of the efficient, one-dimensional contour-following algorithm (Lewis et al. 1993; Witt 1993), where the images of the locus of a source trajectory are followed and summed to produce a microlensing light curve, has allowed the generation of large samples of statistically independent microlensing light curves (Lewis & Irwin 1995, hereafter Paper I). That paper also presented an analysis of the form of the microlensing amplification probability distribution over a large volume of parameter space, illustrating the insensitivity of this statistic to the details of the mass function at all amplifications.

This paper extends the earlier paper and presents a quantitative study of the variability seen in these microlensing light curves. The paper begins by discussing previous studies of these temporal properties. The structure function is then introduced. This is the statistical tool employed to characterize the microlensing variability. This is followed by an

★E-mail: gfl@ast.cam.ac.uk (GFL)

interpretation of the results, with a comparison to previous studies. The appendix discusses a number of scalings in the microlensing relations, and demonstrates that these are displayed in the light curves generated with the efficient contour-following algorithm.

## 1.1 Microlensing equations

The deflection of a light ray through a field of point masses is described by the normalized microlensing equation,

$$y = \begin{pmatrix} 1-\gamma & 0 \\ 0 & 1+\gamma \end{pmatrix} x - \sigma_c x - \sum_{i=1}^{N_*} m_i \frac{(x-x_i)}{(x-x_i)^2}, \tag{1}$$

where $y$ and $x$ are angular coordinates in the source and image plane, respectively (Schneider, Ehlers & Falco 1992). Here, $\gamma$ is the shearing of the bundles of light rays due to the large-scale matter distribution, and $\sigma_c$ is the effect of a local smooth matter component. The final term refers to the contribution due to a surface density, $\sigma_*$, of $N_*$ point masses, each with a mass $m_i = M_i/M_\odot$. These densities are normalized with respect to the critical lensing surface mass density

$$\Sigma_{cr} = \frac{c^2}{4\pi G} \frac{D_{os}}{D_{ol}D_{ls}}, \tag{2}$$

where $D_{os}$, $D_{ol}$ and $D_{ls}$ are the observer–source, observer–lens and lens–source angular diameter distances, respectively. The distances are in units of an angular Einstein (or critical) radius $b_\odot$, of a solar-mass star, which is given by

$$\Sigma_{cr}\pi b_\odot^2 D_{ol}^2 = M_\odot. \tag{3}$$

The theoretically expected average amplification with these parameters is given by

$$\mu_{th} = \frac{1}{(1-\sigma_* - \sigma_c)^2 - \gamma^2}. \tag{4}$$

## 1.2 Effective microlensing velocity

The rate of these microlensing fluctuations is dictated by the effective velocity of the complex lensing amplifications structure crossing over the source plane. This velocity is a combination of the velocities of the source, lens and the observer. Kayser et al. (1986) expressed the resultant velocity as

$$V = \frac{v_s}{1+z_s} - \frac{v_l}{1+z_l}\frac{D_{os}}{D_{ol}} + \frac{v_o}{1+z_l}\frac{D_{ls}}{D_{ol}}, \tag{5}$$

where $v_i$ are the velocities perpendicular to the line of sight, of the source (at a redshift of $z_s$), lens (at $z_l$) and observer.

## 1.3 Motivation and previous results

In general, two separate approaches are used to study the temporal structure in synthetic microlensing light curves. The first of these employs a characterization of individual events in a synthetic light curve. This analysis is sensitive to short-time-scale variability, which is dependent upon the

size and form of the source being lensed (Wambsganss 1990). A second approach is to measure the longer time-scale characteristics of the variability. This depends on large-scale structure in the light curve and is less dependent on the nature of the source. This will be the focus of this paper.

By taking various cuts across amplification maps, Wambsganss was able to generate a number of microlensing light curves for various macrolensing parameters (Wambsganss, Paczyński & Katz 1990). From these light curves, he could calculate the autocorrelation function as a measure of the variability. This is defined as

$$\Gamma(\Delta t) = \frac{\langle \mu(t) \times \mu(t+\Delta t) - \langle \mu \rangle^2 \rangle}{\langle \mu^2 \rangle - \langle \mu \rangle^2}, \tag{6}$$

where $\Delta t$ is the 'lag', and $\sqrt{\langle \mu^2 \rangle - \langle \mu \rangle^2} = \sigma_\mu$ is the standard deviation of the signal. This function is normalized to unity at $\Delta t = 0$, and tends to zero as $\Delta t \to \infty$. The 'correlation time', $\Delta t_{corr}$, was defined such that $\Gamma(\Delta t_{corr}) = 0.5$. The correlation length, $\eta_{corr}$, is given by

$$\eta_{corr} = |V|\,\Delta t_{corr}, \tag{7}$$

where $V$ is the effective velocity across the source plane (equation 5). Wamsbganss calculated the correlation length for several microlensing scenarios, and found that this measure depended on the orientation of the source trajectory relative to the shear, $\theta$, such that

$$\eta_{corr}(\theta) = \eta_c \frac{a_{00} a_{90}}{\sqrt{(a_{00}\sin\theta)^2 + (a_{90}\cos\theta)^2}}, \tag{8}$$

where $a_{00} = |1 - \sigma_* - \gamma|$ and $a_{90} = |1 - \sigma_* + \gamma|$, the eigenvalues of the amplification tensor. For later comparison we note that this can be rewritten as

$$\eta_{corr}(\theta) = \eta_c \frac{R}{\sqrt{R^2 \sin^2\theta + \cos^2\theta}}; \qquad R = \frac{a_{00}}{a_{90}}. \tag{9}$$

## 2 MICROLENSING LIGHT-CURVE SAMPLE

For this study a large sample of microlensing light curves were generated using the efficient contour-following algorithm (Lewis et al. 1993; Witt 1993). This method utilizes novel properties of the lensing mapping, namely that the image of an infinite straight line, which represents the locus of a source trajectory, is imaged into a non-linear infinite curve and a series of image loops. Each of these loops crosses at least one star in the field and this enables each loop to be located. This allows the determination of all images at all times. The total light curve is generated by summing each of these individual loop contributions. This method is essentially a one-dimensional contour-following algorithm and allows a more efficient generation of light curves when compared to other contemporary algorithms, such as the backwards ray-tracing technique. Several examples of light curves produced by this technique are presented in Fig. 1. As a further test of the efficacy of this method of generating light curves, we demonstrate in Appendix A how the expected scaling properties of microlensing due to the relative contributions of smoothly distri-
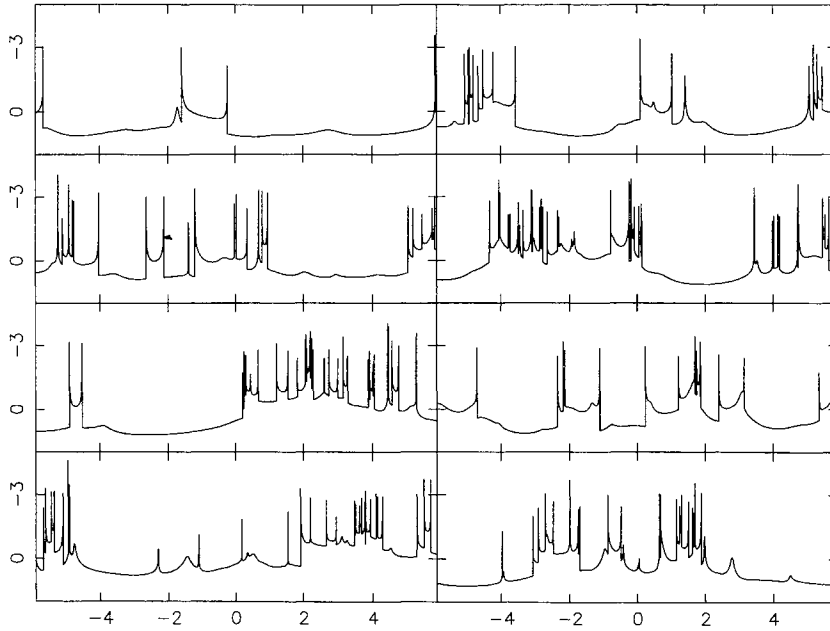
**Figure 1.** An example of several sections of light curves generated with the efficient contouring algorithm. Those in the left-hand panels are for the parameter set $(\sigma_*, \sigma_c) = (0.5, 0.0)$, while those on the right are for $(\sigma_*, \sigma_c) = (0.25, 0.5)$. The x-axis is in Einstein radii, while the y-axis is in magnitudes. In both cases the light curves are for point sources and have been normalized to the theoretical mean magnitude (equation 4).

buted matter, and matter in discrete objects, can be used to verify the effectiveness of the method.

Paper I presented the details of the sample employed in this study, as well as an analysis of the microlensing amplification probability distribution. The first set of light curves were generated for optical depths of $\sigma_* = (0.2, 0.35, 0.5, 0.65, 0.8)$, with no external shear term, i.e., $\gamma = 0.0$. Two mass distributions were employed, per surface density. In the first of these, which is referred to as MSOLAR, all the stars have a mass of 1 $M_\odot$. In the second mass function, SALPETER, the stellar masses were drawn from a Salpeter mass distribution, which is defined to be

$$f(m) \, dm \propto m^\beta \, dm, \tag{10}$$

with $\beta = -2.35$, between the limits of $0.1 < m < 1.0 \, M_\odot$. At least 50 light curves, each of 20 Einstein radii in extent, were generated for each sample.

The second set of light curve samples also employed the same $\sigma_*$ range, but employed a non-zero external shear. For each surface density, samples with $\gamma = (0.2, 0.35, 0.5, 0.65, 0.8)$ were generated.

## 3 METHOD

### 3.1 The structure function

Several observational studies have employed structure function analysis as a method to characterize the variability seen in a light curve (Simonetti, Cordes & Heeschen 1985; Hook et al. 1994). For a time-dependent signal, $\mu(t)$, the first-order structure, $\psi(\Delta t)$, is defined to be

$$\psi(\Delta t) = \langle [\mu(t + \Delta t) - \mu(t)]^2 \rangle. \tag{11}$$

This function is related to the correlation function, equation (6), such that,

$$\psi(\Delta t) = 2\sigma_\mu^2 [\Gamma(0) - \Gamma(\Delta t)] \equiv 2\sigma_\mu^2 [1 - \Gamma(\Delta t)]. \tag{12}$$

For the following analysis $T_{1/2}$ is defined to be the rise time of the structure function to half its asymptotic value. Noting that $\psi(\infty) = 2\sigma_\mu^2$, and that $\Gamma(\Delta t_{corr}) = 0.5$, then

$$\frac{\psi(\Delta t_{corr})}{\psi(\infty)} = [1 - \Gamma(\Delta t_{corr})] = 0.5, \tag{13}$$

and it can be seen how $T_{1/2}$ is related to the correlation length, $\Delta t_{corr}$ (equation 6).

For the analysis presented in this paper the discrete structure function, defined as (Hook et al. 1994)

$$\psi_j = \langle |m_{i+j} - m_i| \rangle, \tag{14}$$

was employed. Here, $m$ is a magnitude, and is defined to be

$$m = -2.5 \log \mu, \tag{15}$$

where $\mu$ is the microlensing induced amplification. An advantage of structure functions is that they do not depend on prior estimates of the mean amplification, and a further advantage of using the absolute difference is that it is more robust to outlying points than the more conventional quadratic difference function. The lessened susceptibility to sharp variations, which occur for point sources, is useful for measuring just the overall trend of the structure function.[1]

[1] Since there is no simple scaling relationship between the structure functions defined by equations (11) and (14), we performed a series of tests, using a subset of the microlensing light-curve sample, to investigate the derived properties of the two forms. We found no significant differences in the temporal trends, and conclude that physical properties deduced from either structure function would be the same. In particular, in a later section investigating the dependence of the time-scale on geometrical effects, we find no difference in the conclusions arrived at using either form.

228   *G. F. Lewis and M. J. Irwin*

```
   0      1      2      3      4      5     12     19     25

      1      1      1      1      1      7      7      6
      2      2      2      2      8     14     13
      3      3      3      9     15     20
             4      4     10     16     21
             5     11     17     22
                   12     18     23
                   19     24
                          25
```

**Figure 2.** A nine-point Golomb ruler. The top row of numbers represents the ruler points, while the triangle below presents the difference between various pairs of ruler points. As can be seen, all separations up to 25 are present, with 1, 2, 3, 4 and 7 being measured more than once.

The structure function was evaluated by sampling each light curve with a series of simulated 'observations'. For the analysis presented in this paper the sample positions were chosen to provide regular sampling in $\Delta t$. This provides a uniform data set to which a functional form for the structure function can be readily evaluated without giving undue weight to particular regions.

### 3.2 Regular sampling in $\Delta t$: Golomb's ruler

The positions of data points in observed microlensing quasars is very heavily biased due to observational factors, such as the position of the Sun, weather conditions and the allocation of telescope time. When a correlation, or structure function, analysis is applied to data sampled in this way, in general, provides very poor coverage in $\Delta t$ space: see Fig. 9 for the coverage in $\Delta t$ for the observed light curves of the lensed quasar system. The theoretical light curves presented in this section were sampled with 'observations' corresponding to the spacing on a Golomb ruler (Dewdney 1985, 1986). Although these rulers sample light curves in an irregular way, they provide a regular sampling in $\Delta t$. Such a coverage allows a functional form to be fitted to the $\Delta t$ statistic in a robust way. It should be noted that for a required, fixed spacing, $\delta t$, in $\Delta t$ space, a Golomb ruler sampling will provide a complete set of data points, such that

$$\Delta t_i = i \times \delta t \qquad (16)$$

for the minimum number of observations in $t$.

Golomb rulers define an ordered numeric sequence such that the difference between any two points on the ruler is not repeated. This is most easily illustrated by example. Consider a ruler with four marks upon it, at 0, 1, 4 and 6 units. Any distance between 0 and 6 units is measurable. This is, in fact, the maximum size for a perfect Golomb ruler, and all rulers greater than this length cannot uniquely measure all the integer measures between the start and end of the ruler. Mathematicians, therefore, search for optimum rulers. Like perfect rulers, these do not repeat any differences between points, but a number of measures are not possible. Optimal rulers with 19 marks, able to measure 171 distances out on a total ruler of length 246 units, have been found (Dollos, Rankin & McCracken 1996). There is no general method used in the construction of these rulers, and possible combinations are validated by numerical searches.

For the analysis presented in this paper a form of minimal Golomb rulers are employed. These rulers are almost perfect, containing the minimum number of repetitions of a particular separation. As with all the kinds of ruler, the validation of minimal Golomb rulers must be checked via numerical techniques. An example of the Golomb's ruler employed in this analysis is presented in Fig. 2.

### 3.3 Functional fit

The resultant structure functions for each of the samples of light curves were fitted with an analytic function of the form

$$\psi(\Delta t) = A[1 - e^{f(\Delta t)}], \qquad f(\Delta t) = -\left(\frac{\Delta t}{T_c}\right)^\beta. \qquad (17)$$

This function has the limits $\psi(0) = 0$ and $\psi(\infty) = A$, where $A$ is the asymptotic limit presented in Paper I. This functional form has the advantage that it has an asymptotic limit, $A$, that can be derived directly from the convolution of the microlensing amplification probability distribution, and is therefore not a free parameter in the temporal fits. The structure function is then completely characterized by three parameters, $A$, $\beta$ and $T_c$, where $\beta$ parametrizes the overall degree of curvature of the structure function, while $T_c$ is the time-scale over which the structure function rises to $(1 - e^{-1}) \sim 0.632$ of the asymptotic value. Another useful measure of the lensing time-scale is given by $T_{1/2}$, which is the time-scale over which the structure function rises to $0.5A$, as described in Section 3.1. This is defined to be

$$T_{1/2} = (\ln 2)^{1/\beta} T_c. \qquad (18)$$

Each structure function was also fitted with a polynomial of the form

$$\psi(\Delta t) = \sum_{i=1}^{5} k_i (\Delta t)^{1/i}, \qquad (19)$$

where the constants, $k_i$, were determined with a least-squares minimization technique. This functional fit was solely used to establish the characteristic time-scale $T_{1/2}$ in an alternative way.

## 4   RESULTS

### 4.1   Samples with no shear

The first row in Table 1 presents the asymptotic value, $A$, of the structure function for the samples with no shear. The fitted parameters: $T_{exp}$, $\beta$ and $T_{1/2}$, using these values, are presented in Fig. 3. It is immediately apparent from these

© 1996 RAS, MNRAS **283**, 225–240

**Table 1.** The asymptotic value of the structure function as derived in Paper I. These values are drawn directly from a convolution of the amplification probability distribution. Here, $\sigma_*$ is the surface density in point-mass lenses, and $\gamma$ is the global shear.

| $\gamma \backslash \sigma_*$ | 0.20 | 0.35 | 0.50 | 0.65 | 0.80 |
|---|---|---|---|---|---|
| 0.00 | 0.36 | 0.61 | 0.77 | 0.83 | 0.72 |
| 0.20 | 0.40 | 0.64 | 0.80 | 0.78 | |
| 0.35 | 0.44 | 0.71 | 0.76 | | 0.72 |
| 0.50 | 0.56 | 0.76 | | 0.82 | 0.90 |
| 0.65 | 0.72 | | 0.96 | 1.03 | 0.97 |
| 0.80 | | 1.14 | 1.13 | 1.05 | 0.96 |

figures that curvature of the fit, $\beta$, is independent of the mass function of the lensing objects, but it is strongly dependent upon the value of the surface mass density, $\sigma_*$. The dashed line represents a functional fit of the form,

$$\beta = 0.882 - 0.138\sigma_* - 0.618\sigma_*^2. \tag{20}$$

### 4.2 Samples with shear

The asymptotic values of the structure function for the samples with shear are presented in Table 1. The results of the fitting for these samples are presented in Table 2. It was found that the polynomial form gave more reliable estimates of the characteristic time-scale than parametric representation, using equation (17); consequently, all time-scales were estimated using the former. For the various $\sigma_*$ and $\gamma$ samples, Table 2 presents $T_{1/2}$ as a function of the shear orientation $\theta$.

The third, fourth and fifth columns present $T_{1/2}$ for shear orientations $\theta = 0°$, 45° and 90° respectively, in units of Einstein radii in the source plane. Each of these columns contains two numbers, the top is for the SALPETER samples, while the lower values are for MSOLAR cases. The final column in this table presents the mean of $T_{1/2}$ for the SALPETER cases divided by the equivalent MSOLAR cases.

## 5 INTERPRETATION

### 5.1 Variability and $\langle m \rangle$

The Einstein radius for a star of mass $m$ can be seen, by equation (3), to be proportional to $\sqrt{m}$. As the crossing time of this radius defines the time-scale that an individual star has 'influence' on a light curve, it would be expected that the time-scale of the variability also scales as $\sqrt{m}$. For an ensemble of masses the variability will scale as the square root of the characteristic lensing mass, which can be taken to be the mean of the mass distribution. This was shown by Witt, Kayser & Refsdal (1993), who studied the mean
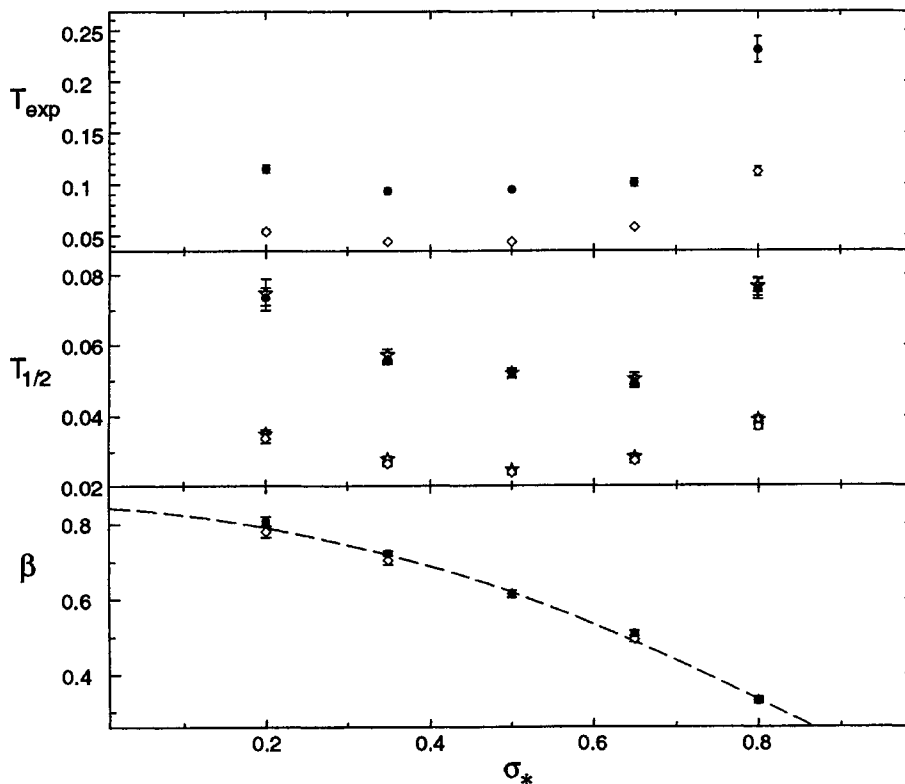


**Figure 3.** These three panels present the fit parameters for the samples with no external shear. The open points in the panels indicate the result for the SALPETER sample, while the filled points are for the MSOLAR sample. The error bars are the standard deviation of 50 realizations of the structure function, for each parameter set. The stars in the figure for $T_{1/2}$ (equation 18) are drawn from the polynomial fit of the data points.

**Table 2.** For the various macrolensing parameters this table presents $T_{1/2}(\theta)$. The first two columns contain the macro parameters, $\sigma_*$ and $\gamma$, while the next six contains the $T_{1/2}(\theta)$ for $\theta = 0°$, 45° and 90°. The first three are for the SALPETER samples (S), while the second three are for the MSOLAR samples. The final column contains the time-scale for the MSOLAR data points divided by the value from the SALPETER values, averaged over the three shear directions, with $\sigma_{n-1}$ errors. The error in the individual values of $T_{1/2}$ is estimated to be 0.03.

| $\sigma_*$ | $\gamma$ | $T_{\frac{1}{2}}^S(0°)$ | $T_{\frac{1}{2}}^S(45°)$ | $T_{\frac{1}{2}}^S(90°)$ | $T_{\frac{1}{2}}^M(0°)$ | $T_{\frac{1}{2}}^M(45°)$ | $T_{\frac{1}{2}}^M(90°)$ | $\left\langle T_{\frac{1}{2}}^M/T_{\frac{1}{2}}^S \right\rangle \pm \sigma_{n-1}$ |
|---|---|---|---|---|---|---|---|---|
| 0.20 | 0.20 | 0.23 | 0.27 | 0.47 | 0.48 | 0.59 | 0.88 | 2.05 ± 0.13 |
| 0.20 | 0.35 | 0.16 | 0.22 | 0.39 | 0.37 | 0.45 | 0.99 | 2.30 ± 0.25 |
| 0.20 | 0.50 | 0.12 | 0.18 | 0.33 | 0.28 | 0.35 | 0.68 | 2.11 ± 0.20 |
| 0.20 | 0.65 | 0.10 | 0.13 | 0.29 | 0.18 | 0.25 | 0.53 | 1.85 ± 0.06 |
| 0.35 | 0.20 | 0.21 | 0.26 | 0.29 | 0.44 | 0.54 | 0.63 | 2.12 ± 0.05 |
| 0.35 | 0.35 | 0.17 | 0.22 | 0.32 | 0.33 | 0.40 | 0.74 | 2.02 ± 0.26 |
| 0.35 | 0.50 | 0.10 | 0.14 | 0.27 | 0.22 | 0.26 | 0.50 | 1.97 ± 0.20 |
| 0.35 | 0.80 | 0.10 | 0.13 | 0.28 | 0.19 | 0.26 | 0.56 | 1.97 ± 0.06 |
| 0.50 | 0.20 | 0.21 | 0.22 | 0.29 | 0.43 | 0.47 | 0.59 | 2.07 ± 0.06 |
| 0.50 | 0.35 | 0.13 | 0.16 | 0.25 | 0.25 | 0.33 | 0.46 | 1.94 ± 0.11 |
| 0.50 | 0.65 | 0.11 | 0.14 | 0.25 | 0.29 | 0.27 | 0.57 | 2.28 ± 0.35 |
| 0.50 | 0.80 | 0.13 | 0.16 | 0.34 | 0.25 | 0.34 | 0.66 | 2.02 ± 0.14 |
| 0.65 | 0.20 | 0.21 | 0.25 | 0.34 | 0.41 | 0.50 | 0.63 | 1.94 ± 0.08 |
| 0.65 | 0.50 | 0.11 | 0.14 | 0.20 | 0.21 | 0.26 | 0.41 | 1.94 ± 0.20 |
| 0.65 | 0.65 | 0.14 | 0.19 | 0.31 | 0.28 | 0.32 | 0.55 | 1.82 ± 0.16 |
| 0.65 | 0.80 | 0.15 | 0.19 | 0.31 | 0.28 | 0.34 | 0.69 | 1.96 ± 0.23 |
| 0.80 | 0.35 | 0.13 | 0.15 | 0.20 | 0.24 | 0.32 | 0.41 | 2.01 ± 0.15 |
| 0.80 | 0.50 | 0.14 | 0.18 | 0.26 | 0.27 | 0.33 | 0.45 | 1.83 ± 0.10 |
| 0.80 | 0.65 | 0.17 | 0.18 | 0.29 | 0.30 | 0.36 | 0.49 | 1.82 ± 0.16 |
| 0.80 | 0.80 | 0.17 | 0.20 | 0.30 | 0.33 | 0.37 | 0.68 | 2.02 ± 0.22 |

caustic crossing rate, for two separate mass functions in models of the Huchra lens. Simulations incorporating a low-mass stellar component showed systematically more caustic crossings per Einstein radius, when compared to a sample with only higher mass stars.

To investigate this predicted behaviour, several more microlensing samples were generated for the case where $\sigma_* = 0.5$, with no external shear. The details of these samples are presented in Table 3, and are described fully in Paper I.

With a delta-function mass distribution the mean mass is the mass of any of the individual stars, while for the Salpeter

mass function, the distribution of masses is dominated by stars at the lower bound. It may be argued, therefore, that $\langle m \rangle$ is not the only possible characteristic moment that could describe the global temporal behaviour caused by the mass function distribution. To investigate this further, several additional microlensing light-curve samples were generated. These were chosen to have a uniform mass function,

$$f(m)\, \mathrm{d}m \propto m^0\, \mathrm{d}m, \qquad (21)$$

between an upper and lower mass limit. These possess no particular characteristic mass, unlike the delta function and

**Table 3.** The additional light curves samples at various mass distributions, generated to determine the dependence of the variability on $\langle m \rangle$. All masses are in solar units. Delta refers to samples where all stars were of the same mass, while Salpeter refers to stars with masses drawn from a Salpeter mass distribution (equation 10). Uniform denotes stellar masses drawn from a uniform mass function equation (21) between the indicated limits. The determination of the number of stars used in a simulation, $N_*$, is described in Lewis et al. (1993). Note that, as the duration of a light curve varied between the samples, this number is not a monotonic function of the optical depth to microlensing; rather it is illustrative of the parameter range accessible to the simulation technique. The length of each light curve, in unit of Einstein radii (equation 3) is presented in column $L_*$.

| Mass Function | Mass Limits | $\langle m \rangle$ | $N_*$ | $L_*$ |
|---|---|---|---|---|
| Delta | 1.0 | 1.0 | 989 | 20 |
| Salpeter | $0.1 < M < 1.0$ | 0.223 | 2621 | 20 |
| Delta | 0.3 | 0.3 | 83912 | 200 |
| Delta | 10. | 10. | 2915 | 200 |
| Salpeter | $0.3 < M < 10.$ | 0.825 | 33345 | 200 |
| Salpeter | $0.3 < M < 1.0$ | 0.495 | 1477 | 20 |
| Salpeter | $1.0 < M < 100$ | 3.084 | 1866 | 20 |
| Salpeter | $0.05 < M < 100$ | 0.179 | 13313 | 20 |
| Uniform | $0.1 < M < 1.0$ | 0.45 | 1457 | 20 |
| Uniform | $0.1 < M < 2.0$ | 0.95 | 1109 | 20 |
| Uniform | $0.1 < M < 6.0$ | 2.95 | 779 | 20 |
| Uniform | $0.1 < M < 10.$ | 4.95 | 686 | 20 |
| Uniform | $0.1 < M < 20.$ | 9.95 | 595 | 20 |

Salpeter mass case, which are dominated by a single mass value. At least 50 light curves, of length 20 Einstein radii, were generated for samples with differing mass limits. The details of these samples are presented in Table 3.

Fig. 4 presents the value of the rise time, $T_{1/2}$, as a function of the mean mass, $\langle m \rangle$, for these samples. The dashed line is of the form

$$T_{1/2} = 0.571 \sqrt{\langle m \rangle} . \tag{22}$$

As can be seen, this relation holds over the both the mass range considered in these samples and is independent of the detailed shape of the distribution function.

This scaling in $T_{1/2}$ can be seen in the microlensing samples with an external shear by examining the final column in Table 2. This column presents the time-scale, $T_{1/2}$, for the SALPETER samples divided by the MSOLAR cases. For a particular set of values of $\sigma_*$ and $\gamma$, the value presented is an average of the three shear orientations. If the time-scale is proportional to $\langle m \rangle$, the expected scaling between these two samples is

$$\frac{\langle T_{1/2}^{M}, \gamma = 0 \rangle}{\langle T_{1/2}^{S}, \gamma = 0 \rangle} = \sqrt{\frac{\langle m^{M} \rangle}{\langle m^{S} \rangle}} \approx \sqrt{\frac{1}{0.223}} \sim 2.12 \tag{23}$$

(cf. Table 3), and the values in Table 2 are in good agreement with this.

## 5.2 Variability and shear orientation

Fig. 5 graphically presents the information in Table 2. The points in this figure represent $T_{1/2}(\theta)$ scaled such that

$$T'_{1/2}(\theta) = \frac{T_{1/2}(\theta)}{T_{1/2}(90°)} . \tag{24}$$

When scaled in this way, $T_{1/2}$ is independent of the mass spectrum of the lensing objects. This is due to the $\sqrt{\langle m \rangle}$ scaling discussed previously.

The solid curve is the behaviour of $T_{1/2}(\theta)$ if the action of shear on microlensing produces a purely geometric transformation of the amplification map in the source plane (cf. equation 8). There are obviously substantial departures from this expected form, especially approaching the $\mu = \infty$ diagonal in the $\sigma_*-\gamma$ plane, with the measured form being consistently greater, except for $(\sigma_*, \gamma)$ of $(0.2, 0.2)$ and $(0.8, 0.8)$.

Fig. 6 presents a caustic map for a region of the source plane, with microlensing parameters $(\sigma_*, \sigma_c, \gamma) = (0.35, 0.0, 0.5)$, generated using the backwards ray-tracing technique (Kayser et al. 1986; Schneider & Weiss 1987). There is significant structure in this map, with a preferred direction of clustering due to the influence of the shear term. Due to these long chains of caustic structure a geometrical transformation of this map using equation (8) still possesses a preferred direction of caustic clustering, with the time-scale of variability being dependent upon the orientation of the source trajectory. This illustrates that the addition of a global shear term transforms the caustic map in a highly non-linear fashion, and one should not expect the microlensing time-scale to vary in a simple, geometrical fashion.

It is also apparent that there exists a symmetry in the form of $T'_{1/2}(\theta)$ over the $\sigma_*-\gamma$ plane which occurs when $\gamma \Rightarrow \gamma' = (1 - \sigma_*)$ and $(1 - \sigma_*) \Rightarrow (1 - \sigma'_*) = \gamma$. It is interesting to note that these symmetries are not reflected in the form of the amplification probability distributions (see figs 5 and 6 in Paper I). The transforms also produce the symmetry seen in the form of the geometric solution (the solid curve in Fig. 5). This implies that the relation between the orientation of the shear and $T_{1/2}$ is dependent upn $|1 - \sigma_* \pm \gamma|$, the eigenvalues of the amplification tensor. The moduli of these eigenvalues are invariant under the symmetry transformation above, and hence any function of the eigenvalues and the angle $\theta$ will also be invariant to the transform. In particular, we have found that the geometrical functional form of equation (8), with $R$ empirically defined from the simulations as $T_{1/2}(0°)/T_{1/2}(90°)$ provides as good a parametrization as any. A theoretical study of the nature of this relation is currently underway.

The variation of $T_{1/2}$ with shear orientation can then be described by

$$T_{1/2}(\theta) = C_i \sqrt{\langle m \rangle} \; \frac{R_i}{\sqrt{R_i^2 \sin \theta^2 + \cos \theta^2}} , \tag{25}$$

where $\langle m \rangle$ is the average mass of lensing objects, in units of $M_\odot$, and $C_i$ and $R_i$ are parameters deduced from the simulations. This is similar to the geometric interpretation (equation 8), with the dependence on $\sigma_*$ and $\gamma$ implicit in the
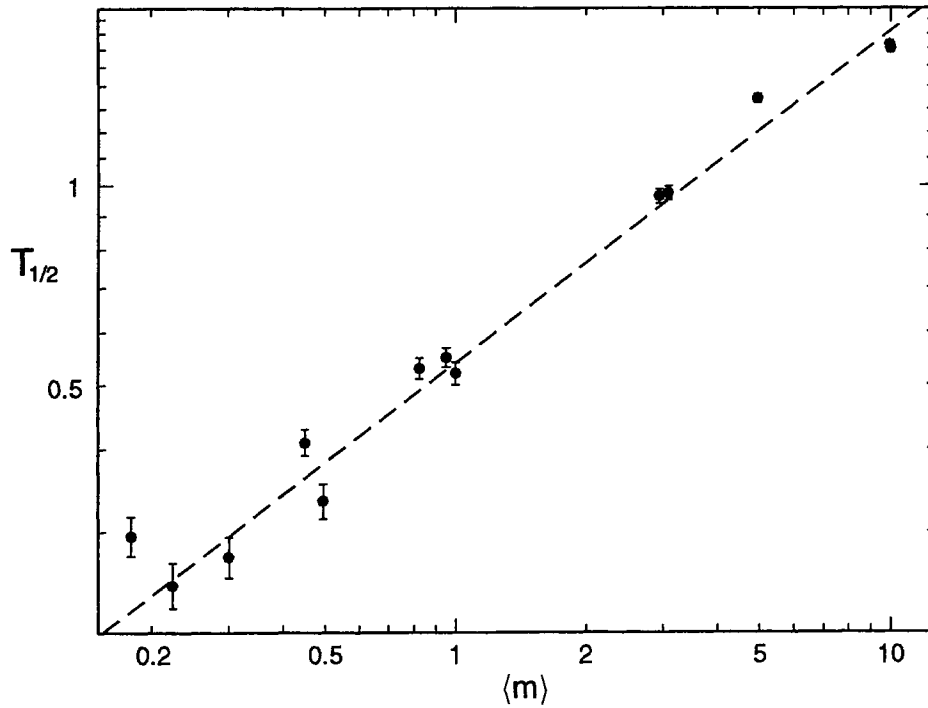
**Figure 4.** The rise-time parameter, $T_{1/2}$, as a function of the mean mass of the lensing objects, for eight different mass profiles. The dashed line represents the expected behaviour of the variability from simple scale arguments. The error bars are drawn from 50 realizations of the time-scale measurement.
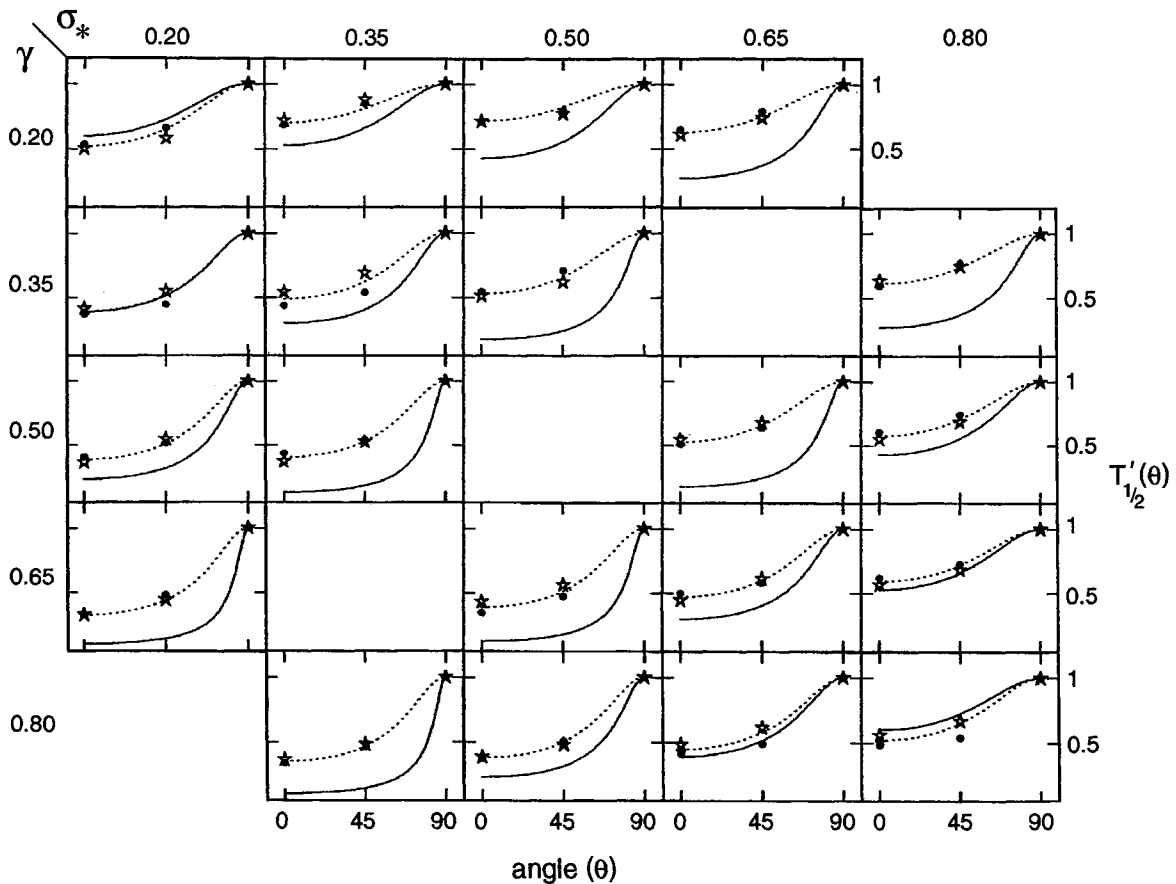


**Figure 5.** $T_{1/2}(\theta)$ for the samples with shear. The time-scales are normalized with respect to $T_{1/2}(90°)$ for each sample. The stars represent the SALPETER light curves, whilst the filled circles represent the MSOLAR sample. The solid line represents the expected effect on $T_{1/2}$ if the application of a shear is interpreted as a purely geometric stretching of the caustic network (cf. equation 8). The dotted line is an equivalent formalization, normalized at $T_{1/2}(0°)$ and $T_{1/2}(90°)$ (see equation 25).

© 1996 RAS, MNRAS **283**, 225–240

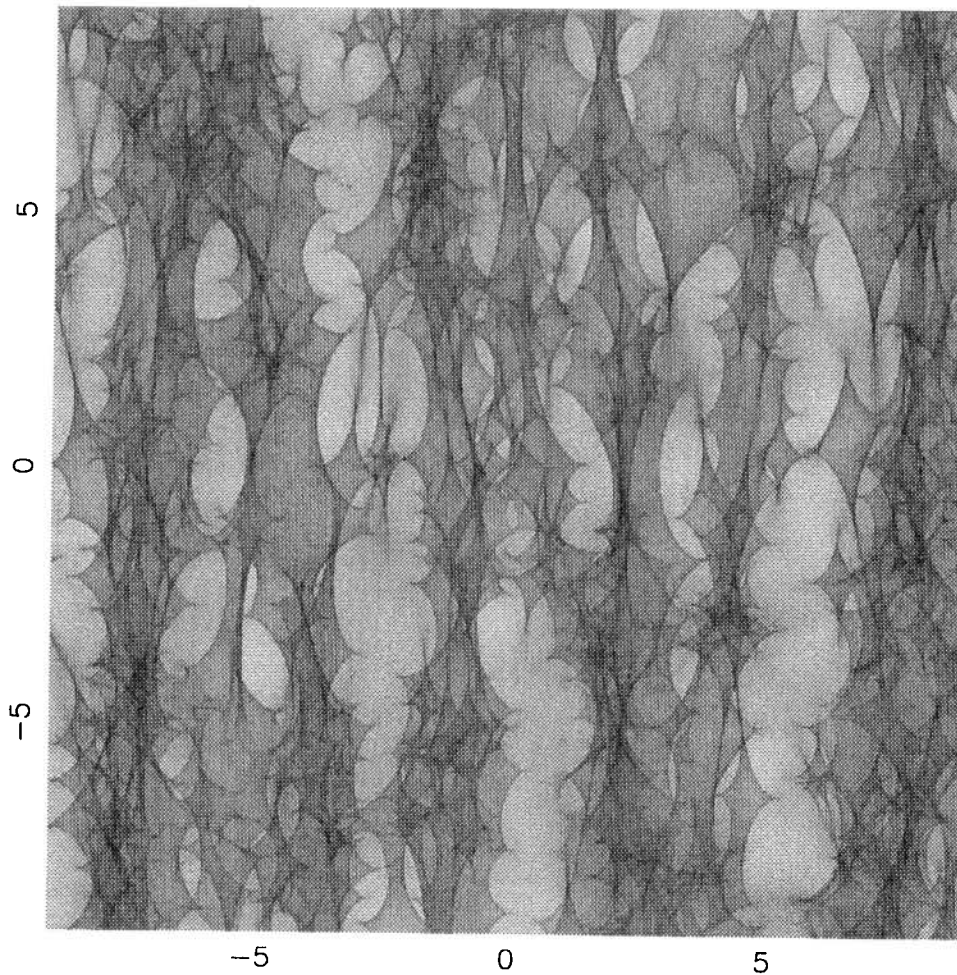© **Royal Astronomical Society • Provided by the NASA Astrophysics Data System**

**Figure 6.** An example of a caustic map generated with the backwards ray-tracing technique. The parameters used for this simulation were $(\sigma_*, \sigma_c, \gamma) = (0.35, 0.0, 0.5)$. All stars in this simulation were of mass 0.386 $M_\odot$, and the box units are in Einstein radii for a solar-mass star (equation 3). For a purely geometrical distortion the expected difference in the time-scale along the $x$- and $y$-axes would be a factor $\sim 7.6$.

**Table 4.** The $C_i$ parameter, used in equation (25), for the samples with shear. $\sigma_*$ runs horiziontally, while $\gamma$ runs vertically.

| $\gamma \backslash \sigma_*$ | 0.20 | 0.35 | 0.50 | 0.65 | 0.80 |
|---|---|---|---|---|---|
| 0.20 | 0.95 | 0.63 | 0.60 | 0.67 | |
| 0.35 | 0.90 | 0.70 | 0.50 | | 0.42 |
| 0.50 | 0.69 | 0.70 | | 0.42 | 0.49 |
| 0.65 | 0.59 | | 0.55 | 0.61 | 0.55 |
| 0.80 | | 0.58 | 0.69 | 0.67 | 0.66 |

**Table 5.** As for Table 4, except that this table presents the $R_i$ parameter in equation (25).

| $\gamma \backslash \sigma_*$ | 0.20 | 0.35 | 0.50 | 0.65 | 0.80 |
|---|---|---|---|---|---|
| 0.20 | 0.52 | 0.70 | 0.72 | 0.63 | |
| 0.35 | 0.40 | 0.49 | 0.53 | | 0.61 |
| 0.50 | 0.38 | 0.49 | | 0.53 | 0.58 |
| 0.65 | 0.32 | | 0.39 | 0.47 | 0.59 |
| 0.80 | | 0.35 | 0.38 | 0.45 | 0.52 |

derived $R_i$. The parameters, $R_i$ and $C_i$, are presented in Tables 4 and 5. The mean difference between this functional form and the values derived from the microlensing sample is 5 per cent, with a maximum deviation of 16 per cent. The symmetry described in the previous paragraph is apparent as a symmetry in the values $R_i$.

To demonstrate this parametric representation, five additional samples of microlensing light curves were generated. The microlensing parameters used were $(\sigma_*, \gamma) = (0.20, 0.65)$, at shear angles of $\theta = 0.0, 22.5, 45.0, 67.5$ and 90.0. Each sample consisted of at least 100 light curves, each

being 60 Einstein radii in extent. The characteristic time-scale, $T_{1/2}(\theta)$, for these samples are presented in Fig. 7. The solid line in this figure represents the parametric fit, employing equation (25) and the numeric values in Tables 4 and 5. The parametric fit accurately reproduces $T_{1/2}$ at the various shear angles.

## 6 MICROLENSING IN Q2237+0305

The lensing system Q2237+0305 consists of four images of a $z = 1.69$ quasar in a cruciform shape centred on the
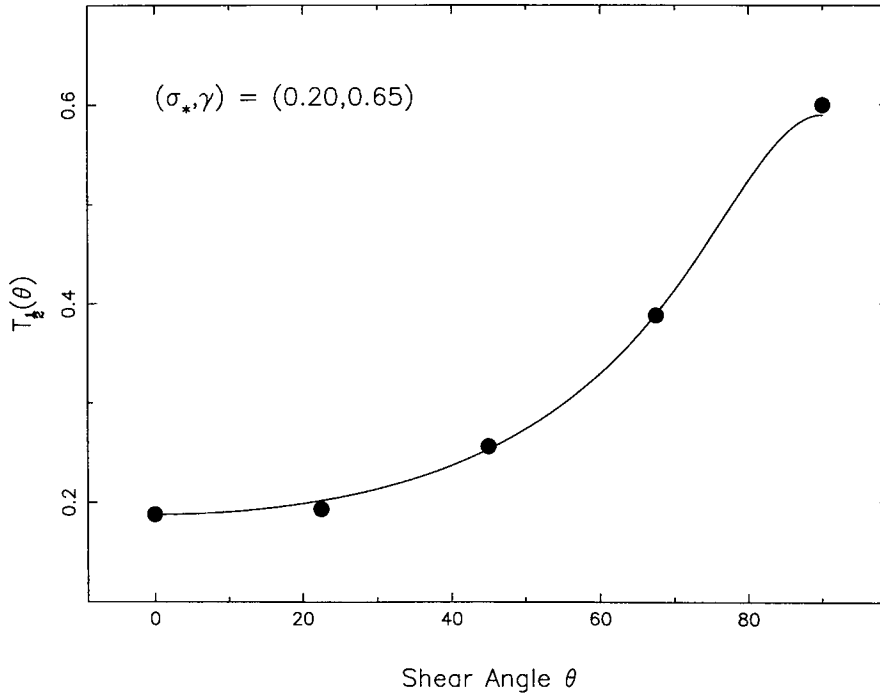
**Figure 7.** The points in this figure present $T_{1/2}(\theta)$ drawn from microlensing light curve samples at various orientations. The curve represents a parametrized fit, employing equation (25) and the numeric values in Tables 4 and 5.

nucleus of a nearby, $z = 0.039$, spiral galaxy. Monitoring of the images in this system revealed the first unambiguous evidence for microlensing occurring in any system (Irwin et al. 1989).

Several models exist that reproduce the observed image configuration and provide estimates of the microlensing parameters at the positions of the images (Kent & Falco 1988; Schneider et al. 1988; Kochanek 1991; Wambsganss & Paczyński 1994). Recently, *Hubble Space Telescope* images of this system were acquired, and these data were used to reproduce the image configuration using a simple mass-traces-light model for the lensing action of the galaxy (Crane et al. 1991; Rix, Schneider & Bahcall 1992). The microlensing parameters from this study, listed in Table 6, were used to generate samples of at least 50 synthetic micro-lensing light curves, each 20 Einstein radii in extent (more details of these samples can be found in Paper I).

### 6.1   Asymptotic values of the structure function

As with the microlensing samples presented in Paper I, the amplification probability distributions for each image of $2237 + 0305$ can be used to calculate the asymptotic value of the structure function. The values for the images were found to be

A $= 0.76$,

B $= 0.77$,

C $= 1.04$,

D $= 0.91$,

independent of the lensing mass function. These values are

**Table 6.** Macrolensing parameters for the four images in Q $2237 + 0305$. These values represent the best solutions of the lens modelling by Rix et al. (1992).

| Image | $\sigma_*$ | $\gamma$ |
|-------|------|------|
| A | 0.41 | 0.47 |
| B | 0.38 | 0.43 |
| C | 0.65 | 0.68 |
| D | 0.59 | 0.56 |

in magnitudes and are employed in the following analysis of the structure function of light curves of the Huchra lens.

### 6.2   Temporal analysis

The structure functions were measured with Golomb ruler sampling in an identical fashion to those presented in Section 3. The resulting data points were fitted with a para-metric function (equation 17), and the time-scale, $T_{1/2}$, was measured via a polynomial fit. The asymptotic values pre-sented in Section 6.1 were used to normalize the structure function as $\Delta t \rightarrow \infty$.

### 6.3   Results

As with the samples with shear presented in Section 4.2, time-scales, $T_{1/2}$, were derived directly from the polynomial fit.

As expected, the variation of the time-scale of the varia-bility with the shear orientation is not described by a simple

geometric transformation (equation 8), although it can be represented by equation (25), with parameters $C_i$ and $R_i$. Table 7 presents $C_i$ and $R_i$ for the simulations presented in this paper. The average deviation of this function from the data points is less than 5 per cent, with the maximum deviation being less than 11 per cent. This can be seen graphically in Fig. 8, which presents the data points for the structure function for the samples presented in this paper, as well as the functional fit outlined above.

### 6.4 Microlensing mass limits in Q 2237 + 0305

Using the values drawn from the temporal analysis of the light curve simulations, coupled with the scaling presented

**Table 7.** The parameters for equation (7) for the simulations for the images of the Huchra lens. $R_i$ is dimensionless, while $C_i$ is in units of Einstein radii in the source plane. These values can be transformed into observed time-scales via equation (7).

|   | $C_i$ | $R_i$ |
|---|---|---|
| A | 0.49 | 0.44 |
| B | 0.61 | 0.44 |
| C | 0.60 | 0.47 |
| D | 0.52 | 0.46 |

in Section 5.1, mass limits can be placed on the mean mass of microlenses in the Q 2237 + 0305 system.

Using equation (3), it can be seen that an Einstein radius for a solar-mass star, projected into the source plane, is

$$\eta_o = 0.05 \, h_{50}^{-1/2} \, \text{pc.} \tag{26}$$

The close proximity of the lensing galaxy ensures a large projected velocity over the source plane, which, considering typical departures from the Hubble flow, gives an effective velocity of 6000 km s$^{-1}$ (Kayser et al. 1986). With this, the crossing time of an Einstein radius is $8.2 \, h_{50}^{-1/2}$ yr.

The orientation of the global shear with respect to the source motion is unknown, but equation (25) increases monotonically as the shear orientation changes between $0°$ and $90°$. With this, the mean mass of the microlensing objects can be seen to be

$$\langle m \rangle = K h_{50} \left( \frac{t_{1/2}}{8.2 \text{ yr}} \right)^2 \left( \frac{|V|}{6000 \text{ km s}^{-1}} \right)^2 \text{M}_\odot, \tag{27}$$

where the factor $K$ is constrained to be

| | |
|---|---|
| A | $4.17 < K < 21.51$ |
| B | $2.69 < K < 13.88$ |
| C | $2.78 < K < 12.57$ |
| D | $3.70 < K < 17.48,$ |

$$\tag{28}$$

depending upon the shear orientation.
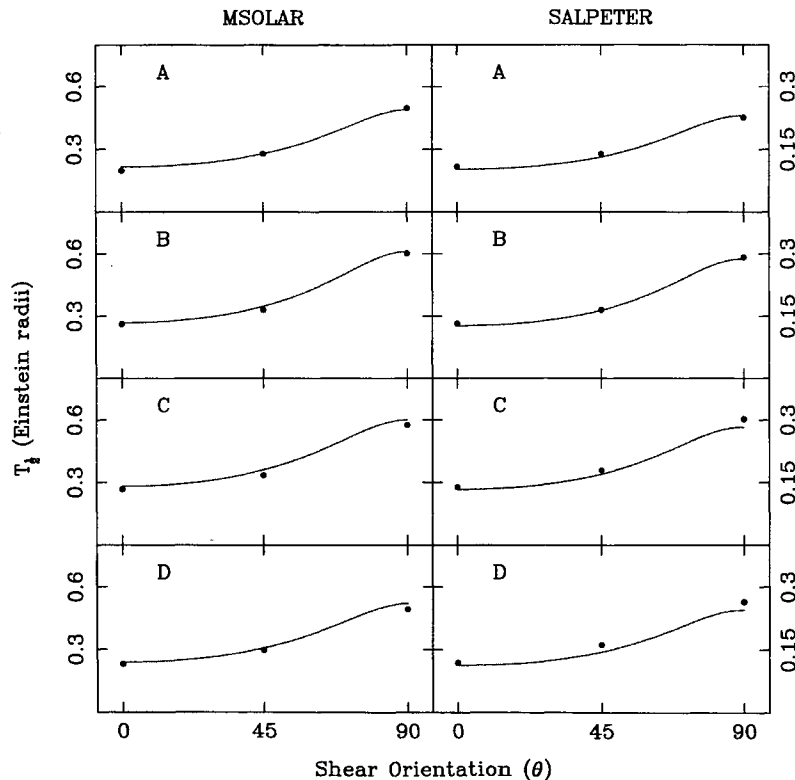
Q 2237 + 0305 has been monitored, at very irregular

**Figure 8.** The predictions, derived from equation (25) using the parameters given in Table 7, (the solid line) accurately describe the data points drawn from the microlensing light curve samples (the filled circles). The left-hand panels are for the MSOLAR samples, while the right-hand panels are for the SALPETER cases. Note the different scales on the y-axes. This is due to the $\sqrt{\langle m \rangle}$ scaling discussed previously.
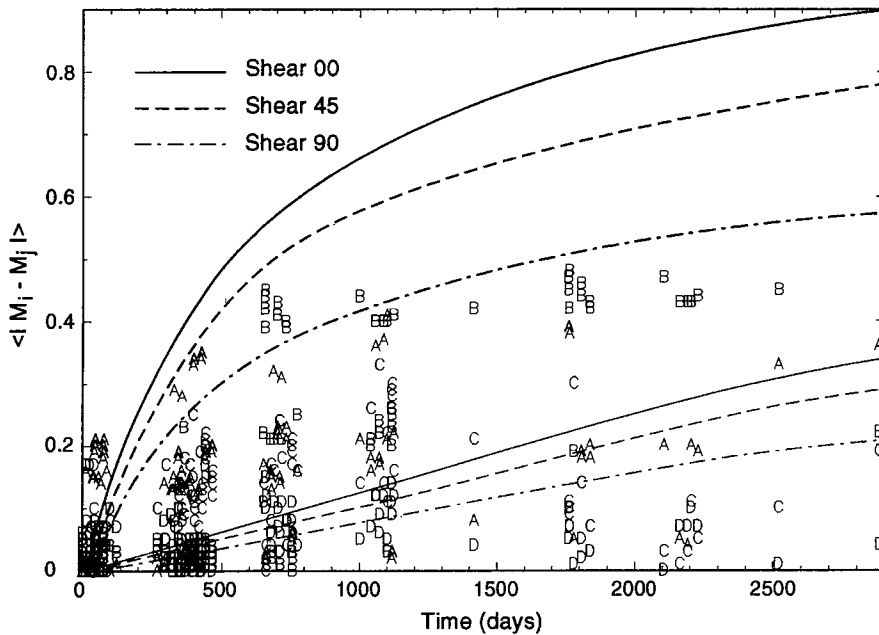
**Figure 9.** The structure function of the observed light curves of the images of Q 2237 + 0305. The letters refer to the individual images. The three curves represent the scaled median structure function, averaged over the four images, for three shear orientations. The thicker lines represent the structure functions for $\langle m \rangle = 0.1$ M$_\odot$, while the thinner set of functions represent the case where $\langle m \rangle = 10$ M$_\odot$.

intervals, for a decade (Lewis, Irwin & Hewett 1995; Lewis et al., in preparation). This short data train does not allow an accurate determination of the form of the structure function, as demonstrated in Fig. 9. Here, the letters refer to the values of the observed structure function, for each of the macrolensed images. To compare these observed values to the synthetic sample, each light curve was smoothed with a Gaussian kernel of radius 0.01 Einstein radii. This is equivalent to a source size of $\sim 10^{15}$ cm, a typical scalesize of a continuum-emitting accretion disc about a supermassive black hole (Rees 1984). The resulting light curves were then sampled with the same frequency as the current observations to establish the median structure function (the median reflects a typical 'observation', rather than the average of a long data train). The structure functions for the MSOLAR sample at each shear orientation were averaged and scaled, and are presented in Fig. 9.[2] The set of structure functions represented by the thicker lines are for the case where $\langle m \rangle = 0.1$ M$_\odot$, while the thinner set of curves have been scaled to represent the case where $\langle m \rangle = 10$ M$_\odot$. These curves bound the data suggesting that, with equation (27), in this lensing system

$$0.1 < \langle m \rangle < 10 \text{ M}_\odot, \qquad (29)$$

($|V| = 6000$ km s$^{-1}$,[3] $h_{50} = 1$), although a substantially longer light curve will be required to place tighter limits on the mean microlensing mass in this system.

[2] The same exercise was conducted for the SALPETER light curve samples, and when accounting for the $\sqrt{\langle m \rangle}$ scaling presented in Section 5.1, the results of this section were unchanged.

[3] It must be noted that this velocity is the effective velocity across the source plane, as given by equation (5). It is a projection of an assumed velocity for the lensing galaxy, which is taken to be 600 km s$^{-1}$, a typical departure from the Hubble flow (Kayser et al. 1986).

## 7 CONCLUSIONS

This paper has presented the temporal analysis of a large sample of microlensing light curves. This was achieved via the evaluation of a structure function. The asymptotic value of this function was measured in Paper I, using the amplification probability distribution. The structure functions were fitted with an analytic model, from which a characteristic time-scale, $T_{1/2}$, the time taken for the structure function to rise to half its asymptotic value, could be derived. The variability time-scale was found to scale with $\sqrt{\langle m \rangle}$, where $\langle m \rangle$ is the mean, or characteristic, mass of the lensing objects. This was shown to hold for various mass distributions.

The variability time-scale is expected to be a function of the direction in which a source moves with respect to the global shear. Wambsganss suggested an analytic formalism for how this relative orientation should affect the time-scale (Wambsganss et al. 1990). This formula represents a simple geometric shearing of the amplification map over the source plane. This paper has shown that this geometric representation does not, in general, represent the scaling of $T_{1/2}$. This is possibly due to non-linear effects in the clustering and merging of the caustic network with the application of an external shear.

Fig. 5 illustrates that there are strong symmetries in the shape of $T_{1/2}$ with shear orientation over the $\sigma_* - \gamma$ plane. These symmetries are those expected if one considers the geometric formalism (equation 8), although the symmetries are not apparent in the amplification probability distributions drawn from the same light curves. This suggests that there exists an underlying physical reason for the symmetries, which is dependent only upon $\sigma_*$ and $\gamma$. This will be a topic of further work.

A similar analysis was applied to simulations of the

© 1996 RAS, MNRAS **283**, 225–240

images of the quadruple quasar Q 2237 + 0305. It was found that these samples exhibited the same behaviour as those in the larger light-curve sample presented in the earlier sections of this paper. These results, coupled with the lensing configuration within this system, allowed the mean mass of microlensing objects to be limited to $0.1 < \langle m \rangle < 10 \, \mathrm{M}_\odot$.

## REFERENCES

Chang K., Refsdal S., 1979, Nat, 282, 561
Crane P. et al., 1991, ApJ, 369, L59
Dewdney A. K., 1985, Scientific American, December, 16
Dewdney A. K., 1986, Scientific American, March, 14
Dollos A., Rankin W. T., McCracken D., 1996, IEEE Transactions on Information Systems, preprint
Hook I. M., McMahon R. G., Boyle B. J., Irwin M. J., 1994, MNRAS, 269, 305
Irwin M. J., Webster R. L., Hewett P. C., Corrigan R. T., Jedrzejewski R. I., 1989, AJ, 98, 1989
Kayser R., Refsdal S., Stabell R., 1986, A&A, 166, 36
Kent S. M., Falco E. E., 1988, AJ, 96, 1570
Kochanek C. S., 1991, ApJ, 373, 354
Lewis G. F., Irwin M. J., 1995, MNRAS, 276, 103 (Paper I)
Lewis G. F., Miralda-Escudé J., Richardson D. C., Wambsganss J., 1993, MNRAS, 261, 647
Lewis G. F., Irwin M. J., Hewett P. C., 1995, in Kochanek C. S., Hewitt J. N., eds, Proc. IAU Symp. 173, Astrophysical Applications of Gravitational Lensing. Kluwer, Dordrecht, p. 241
Paczyński B., 1986, ApJ, 301, 503
Rees M. J., 1984, ARA&A, 21, 471
Rix H. W., Schneider D. P., Bahcall J. N., 1992, ApJ, 104, 959
Schneider P., 1987, ApJ, 319, 9
Schneider P., Weiss A., 1987, A&A, 171, 49
Schneider D. P., Turner E. L., Gunn J. E., Hewitt J. N., Schmidt M., Lawrence C. R., 1988, AJ, 95, 1619
Schneider P., Ehlers J., Falco E. E., 1992, Gravitational Lenses. Springer-Verlag, Berlin
Simonetti J. H., Cordes J. M., Heeschen D. S., 1985, ApJ, 296, 46
Wambsganss J., 1990, PhD thesis, Univ. München
Wambsganss J., 1992, ApJ, 386, 19
Wambsganss J., Paczyński B., 1994, AJ, 108, 1156
Wambsganss J., Paczyński B., Katz N., 1990, ApJ, 352, 407
Witt H.-J., 1993, ApJ, 403, 530
Witt H.-J., Kayser R., Refsdal R., 1993, A&A, 268, 501

## APPENDIX A: MICROLENSING AND SCALING RELATIONS

### A1  Introduction

Several authors have considered the effect of the screen of smoothly distributed matter over the microlensing region (Kayser et al. 1986; Paczyński 1986; Schneider 1987). This

**Table A1.** The details of the microlensing samples presented in this appendix. Here, $N_*$ is the number of stars used in each simulation. The mean amplification of each sample is $\langle \mu \rangle$, while the theoretical value is $\mu_{\mathrm{th}}$ (equation 4).[4]

| $\sigma_*$ | $\sigma_c$ | $\gamma$ | $N_*$ | $\langle \mu \rangle$ | $\mu_{th}$ |
|------|------|------|------|------|------|
| 0.50 | 0.00 | 0.00 | 989 | 3.86 | 4 |
| 0.25 | 0.50 | 0.00 | 1392 | 15.60 | 16 |

matter, $\sigma_c$ in equation (1), is assumed to be uniform over the region of stars that have influence over the source during the period of the light curve. The matter can be baryonic gas or dust, or a smooth distribution of non-baryonic matter. It was shown that such a non-zero smooth matter component, $\sigma_c$, rescales the parameters $\sigma_*$ and $\gamma$ in the microlensing equation (equation 1), such that

$$(\sigma_*, \sigma_c, \gamma) \Rightarrow (\tilde{\sigma}_*, 0, \tilde{\gamma}) = \left( \frac{\sigma_*}{1-\sigma_c}, \, 0, \, \frac{\gamma}{1-\sigma_c} \right). \quad \text{(A1)}$$

This transformation also rescales the mean theoretical amplification, as well as the source and lens plane scale-lengths. These are

$$(\xi_o, \eta_o, \mu) \Rightarrow (\tilde{\xi}_o, \tilde{\eta}_o, \tilde{\mu}) = \left[ \sqrt{|1-\sigma_c|}\, \xi_o, \, \frac{\eta_o}{\sqrt{|1-\sigma_c|}}, \, \frac{\mu}{(1-\sigma_c)^2} \right], \quad \text{(A2)}$$

where $\eta_o = \mathrm{b}_\odot D_{os}$ and $\xi_o = \mathrm{b}_\odot D_{ol}$, and are the physical size of Einstein radii in the source and lens plane without a smooth matter component. Once these scaling factors have been taken into account, the resultant microlensing properties of the two cases must be equivalent.

### A2  The microlensing samples

To examine the parameter scalings, two samples of light curves were generated using the efficient contouring algorithm (Lewis et al. 1993; Witt 1993). The first sample was generated with the parameter set $(\sigma_*, \sigma_c) = (0.5, 0)$, the second with $(\sigma_*, \sigma_c) = (0.25, 0.5)$. All the stars in these simulations were of $1 \, \mathrm{M}_\odot$, and the external shear $\gamma = 0$. In each case a total of 50 light curves of length 20 Einstein radii were generated. The number of stars and the mean amplifications of these samples are presented in Table A1. Several examples of the light curves for these parameter sets are presented in Fig. 1. These parameter sets are equivalent under the scaling relations presented in Section A1.

[4] In the analysis presented here the measured mean amplification, $\langle \mu \rangle$ is systematically lower than the theoretically expected value, $\mu_{\mathrm{th}}$. If one, however, considers the more extensive sample presented in Paper I, it can be seen that there is a reasonable scatter of $\langle \mu \rangle$ about $\mu_{\mathrm{th}}$. As well as being due to the finite length of the light-curve sample, these values reflect the uncertainty introduced when averaging over sample points drawn from a distribution with an extended tail.
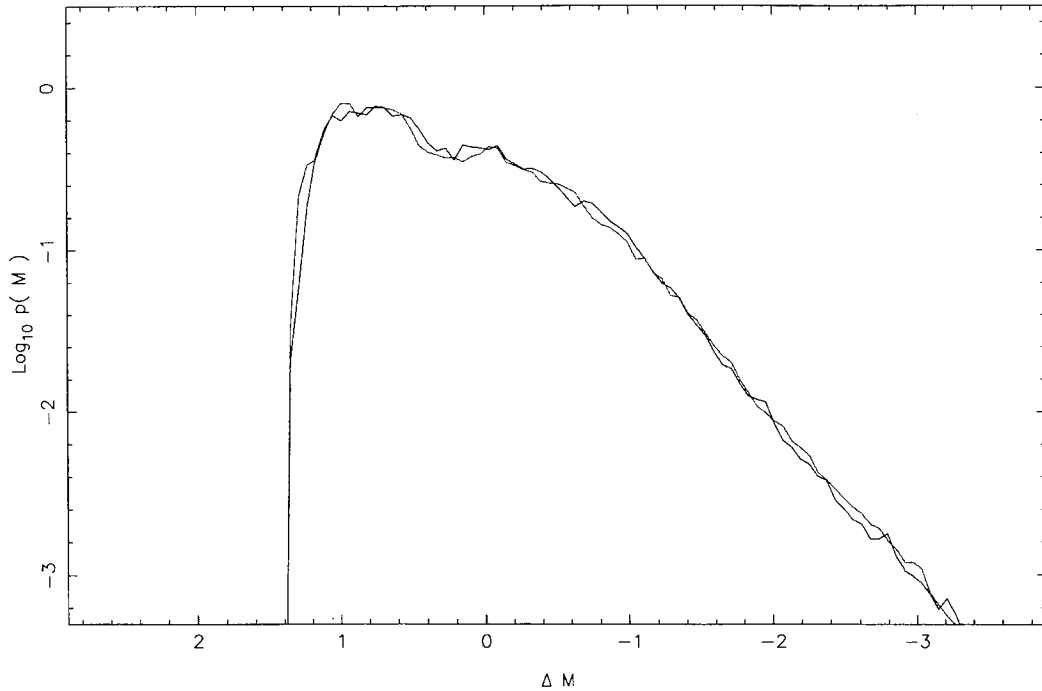
*G. F. Lewis and M. J. Irwin*

**Figure A1.** Amplification probability distributions for the parameter sets $(\sigma_*, \sigma_c, \gamma) = (0.5, 0, 0)$ (dotted line) and $(0.25, 0.5, 0.0)$ (dot-dashed line) respectively. Both distributions are plotted with respect to their theoretical mean. The distributions are the same, in accordance with the scaling relations presented in equations (A1) and (A2).
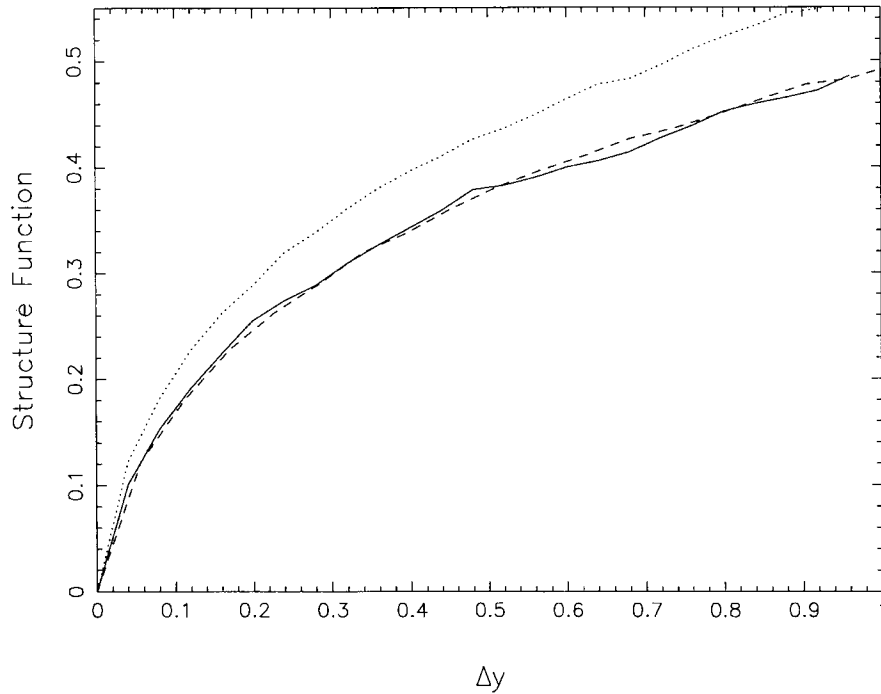


**Figure A2.** The solid line in this figure represents the structure function for the parameter set $(\sigma_*, \sigma_c) = (0.5, 0.0)$, while the dotted line is for $(\sigma_*, \sigma_c) = (0.25, 0.5)$. In both cases the stars were $1\,M_\odot$. The dashed line represents the $(\sigma_*, \sigma_c) = (0.25, 0.5)$ case scaled with the relations presented in equations (A1), and (A2).

## A3 Results

Fig. A1 presents the amplification probability distributions (Wambsganss 1992) for the samples of light curves. These distributions are normalized with respect to their theoreti-cal mean amplification (equation 4). It was demonstrated that for a particular parameter set, $(\sigma_*, \gamma)$, the shape of this distribution is independent of the mass function of the lens-ing objects, although the overall form was found to be strongly dependent upon these macrolensing parameters

© 1996 RAS, MNRAS **283**, 225–240

**Table A2.** The details of the microlensing samples with a global shear term presented in this appendix. Here, $N_*$ is the number of stars used in each simulation. The mean amplification of each sample is $\langle\mu\rangle$, while the theoretical value is $\mu_{th}$ (equation 4).

| $\sigma_*$ | $\sigma_c$ | $\gamma$ | $N_*$ | $\langle\mu\rangle$ | $\mu_{th}$ |
|---|---|---|---|---|---|
| 0.80 | 0.00 | 0.80 | 1443 | 1.55 | 1.67 |
| 0.20 | 0.75 | 0.25 | 2797 | 25.52 | 26.67 |

(Paper I). This figure demonstrates that, when scaled to the theoretically expected mean, the form of these distributions is the same.

If the mass function of the lensing objects is the same between parameter sets, then the temporal structure in the individual light curves of the two samples must be statistically identical when the scaling relations presented in Section A1 are taken into account. As with Section 3, the structure function is employed to study the temporal nature of the light curves. With an effective velocity, $V$, over the source plane, this time is related to a physical distance in the source plane by $\Delta\eta = V\Delta t$. As $\Delta y = \Delta\eta/\eta_o$, the scaling relations presented in Section A1 predict that $\Delta y_{(0.5\,0.0)} = \sqrt{2}\Delta y_{(0.25,\,0.5)}$. The structure function for the two samples of light curves are presented in Fig. A2, with the solid line representing the $(\sigma_*, \sigma_c) = (0.5, 0.0)$ sample, and the dotted line being $(\sigma_*, \sigma_c) = (0.25, 0.5)$. The dashed line

presents this curve with the temporal coordinates scaled by a factor of $\sqrt{2}$. With this scaling the temporal nature of the two samples of light curves match.

## A4 Samples with external shear

A further test was performed by repeating the above analysis with two samples of light curves with a global shear term. The microlensing parameters used to generate these samples are presented in Table A2. In both cases all the stars were 1 $M_\odot$, and each light curve was 20 Einstein radii in duration. Owing to the availability of additional computer processing, each sample consisted of at least 300 individual light curves.

The amplification probability distributions for these samples, normalized to the theoretical mean (equation 4), are presented in Fig. A3. There is an excellent correspondence between the two curves, as expected from the smooth matter scaling relations. The dotted curve in this figure represents the amplification probability distribution for the case where $(\sigma_*, \sigma_c, \gamma) = (0.2, 0, 0.2)$, which can be seen to be quite different in form from the $(\sigma_*, \sigma_c, \gamma) = (0.2, 0.75, 0.2)$ distribution, illustrating that the addition of a smooth matter component can have drastic effects on observed microlensing statistics.

The structure functions for each sample were also measured, and are presented in Fig. A4. The expected temporal scaling for these two samples, from equation (A2), is $\Delta y_{(0.8,\,0.0,\,0.8)} = 2\Delta y_{(0.2,\,0.75,\,0.2)}$. The dashed curve in Fig. A4 represents the structure function for the $(\sigma_*, \sigma_c, \gamma) =$
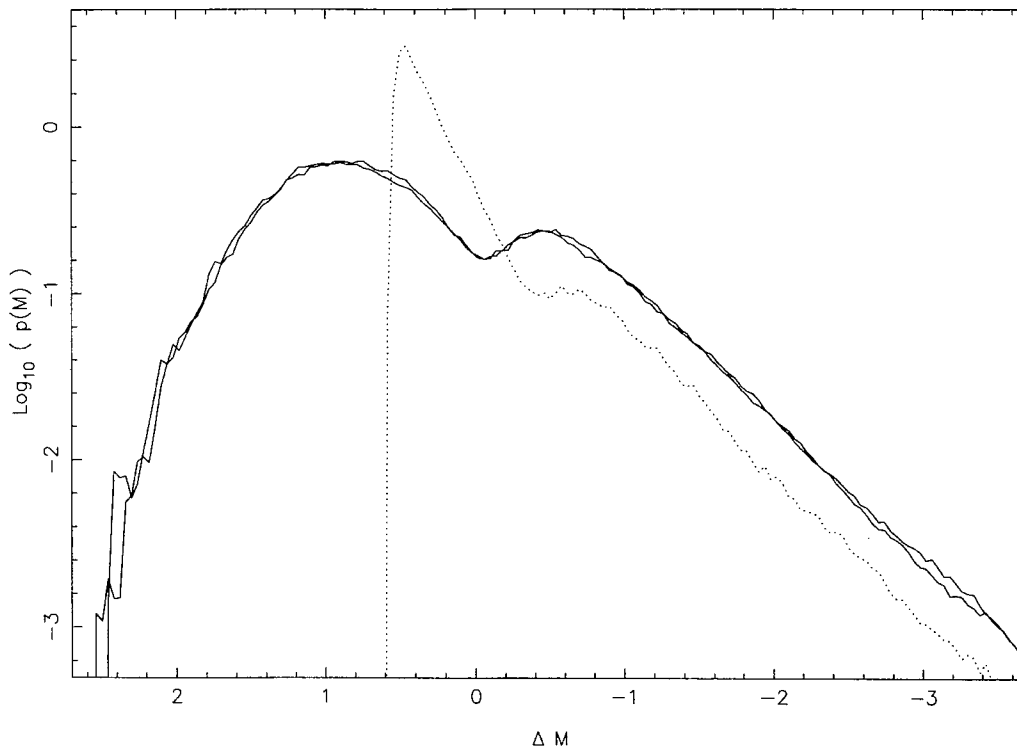
**Figure A3.** The solid lines present the amplification probability distributions for the parameter sets $(\sigma_*, \sigma_c, \gamma) = (0.8, 0, 0.8)$ and $(0.2, 0.75, 0.2)$, respectively. Both distributions are plotted with respect to their theoretical mean. The distributions are the same, in accordance with the scaling relations presented in equations (A1) and (A2). The dotted line in this figure represents the amplifications probability distribution for the case $(\sigma_*, \sigma_c, \gamma) = (0.2, 0, 0.2)$, a comparison case without smooth matter.
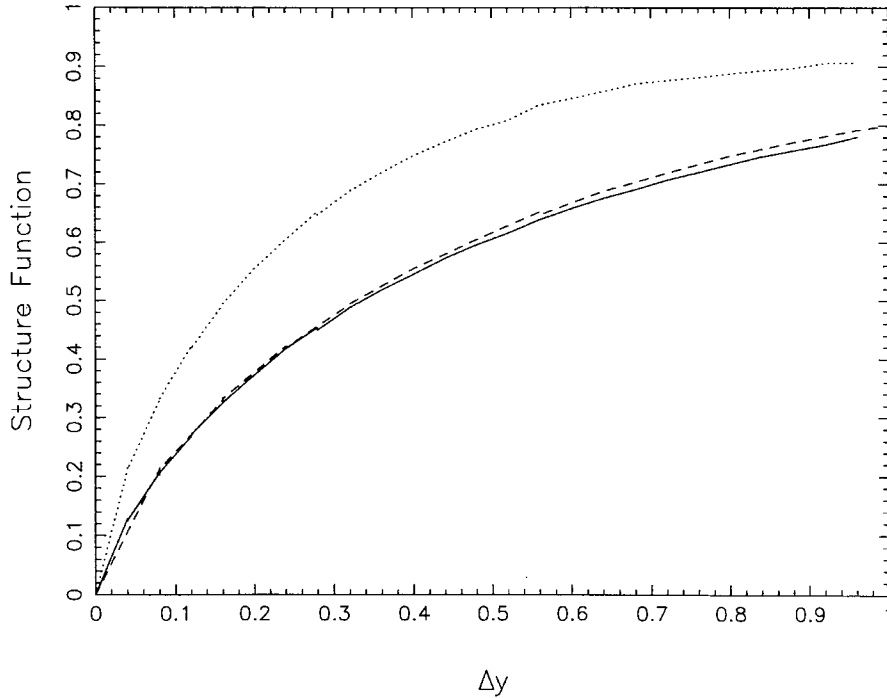
**Figure A4.** The solid line in this figure represents the structure function for the parameter set $(\sigma_*, \sigma_c, \gamma) = (0.8, 0.0, 0.8)$, while the dotted line is for $(\sigma_*, \sigma_c, \gamma) = (0.2, 0.75, 0.2)$. In both cases the stars were 1 $M_\odot$. The dashed line represents the latter case scaled with the relations presented in equations (A1) and (A2).

(0.2, 0.75, 0.2) scaled by this factor. This curve can then be seen to match the structure function for the $(\sigma_*, \sigma_c, \gamma) = (0.8, 0, 0.8)$ sample (solid line).

## A5    Breaking the degeneracy

The scaling factors discussed in this section demonstrate that the addition of a smooth matter component can affect the expected statistics in observed microlensing systems. The following describes how the individual microlensing parameters can be determined by monitoring a known microlensing system.

In simple systems, such as those consisting of an isolated galaxy, modelling of the lensing configuration can determine the total surface mass density, $\sigma = \sigma_c + \sigma_*$, and the global shear, $\gamma$, at the position of each image. Long-term monitoring of the images will allow the determination of the

form of the amplification probability distribution, which can then be compared to those drawn from microlensing simulations. If it is assumed that all matter is in the form of compact objects with no smooth matter component, $\sigma_c = 0.0$, any discrepancy between the theoretical and the observed amplification probability distribution will indicate the presence of smooth matter [subject to the effect of a finite source, which tends to cut off the high amplification tail rather than affecting the overall form of the distribution (Paper I)]. Matching the observed distribution to the equivalent theoretical distribution with no smooth matter component will, as the total surface mass density, $\sigma$, and global shear, $\gamma$, are known, allow the surface mass density in compact objects, $\sigma_*$, to be determined. This information can then be coupled with the measurement of the variability structure function, limiting the mean mass of the microlensing compact objects (Section 6.4).